Electrical Constriction Resistance in Current Collectors of Large-Scale Lithium-Ion Batteries

Peyman Taheri,[a],[*],[z] Abraham Mansouri,[b] Ben Schweitzer,[c] Maryam Yazdanpour,[a],[**] and Majid Bahrami[a]

[a]*Laboratory for Alternative Energy Conversion (LAEC), Mechatronic Systems Engineering, School of Engineering Science, Simon Fraser University, Surrey, British Columbia V3T 0A3, Canada*
[b]*Department of Mechanical Engineering, American University in Dubai, Dubai 28282, United Arab Emirates*
[c]*AllCell Technologies, Chicago, Illinois 60609, USA*

A new two-dimensional model is proposed to describe the electrical conduction in current collectors of prismatic lithium-ion batteries, and to investigate the effects of tab design on voltage drop. Polarization expression for a large-scale lithium-ion cell is determined experimentally and implemented in a numerical analysis to show that reaction current remains approximately uniform when depth-of-discharge is less than 85%. Based on this observation, a compact analytical model is developed to determine bulk and constriction/spreading resistances in current collectors. Moreover, the model predictions are successfully validated through comparisons with experimental data. It is demonstrated that constriction/spreading resistance in current collectors of the considered battery is fairly small; about 10% of the total cell resistance but it is larger than the contribution of bulk resistance which is about 3%. The model confirms that constriction/spreading increase with: decrease in the aspect ratio of the current collector, decrease in the tab width, and increase in the tab eccentricity.
© 2013 The Electrochemical Society. [DOI: 10.1149/2.041310jes] All rights reserved.

Lithium-ion (Li-ion) batteries have become the dominant battery technology for consumer electronics, and most recently, for hybrid-electric vehicles and grid storage, due to several compelling features such as high power and energy densities, high voltage, long cycle life, excellent storage capabilities, and memory-free recharge characteristics.

While Li-ion batteries are growing fast in popularity, their safety and the risk of thermal runaway remains a major concern.[1,2] In this regard, thermal modeling and thermal management of large-scale Li-ion batteries have received increasing attention due to their widespread applications in automotive, military, and aviation industries; for examples of different approaches see Refs. 3–14.

The total heat generation inside Li-ion batteries is the summation of reaction heat, active polarization heat, and ohmic heat.[15–17] While the heat generation due to reaction and active polarization is dictated by the cell chemistry, the ohmic heating is mostly related to electronic conductivity of the materials and architecture of the cell.[18]

One of the key bottlenecks in designing a thermally stable Li-ion battery is rooted in the geometric design of electrodes and current collectors; improper designs result in non-uniformities in current distribution, particularly at high charge and discharge rates.[19,20] At such high-rate circumstances, experimental measurements,[21,22] infrared thermographs,[23,24] electro-thermal models,[25–27] and thermo-electrochemical simulations[28–30] reveal the significant role of ohmic resistance around the current collecting tabs.

With the fast-paced development of numerical methods and computer technology, costly electrochemical simulations for Li-ion batteries have become a common approach in their design and optimization. However, to the authors' best knowledge, lack of an analytical model for the design of current collectors in Li-ion batteries is apparent in the literature. From the computational point of view, analytical solutions are highly on demand because they are continuous in the independent variables, and show explicitly how the parameters of the system are involved. Furthermore, analytical solutions give much insight into a system, which is one of the primary objectives of modeling. Accordingly, in this work, a theoretical model is developed to predict the distributions of potential and current density in current collectors of a large-scale (75 Ah) Li-ion battery. The proposed model is further employed to perform a comprehensive parametric study on the effects of geometrical configuration in ohmic losses. In our analysis, the total ohmic resistance of the battery is split into three components; constriction/spreading resistance, bulk resistance, and electrochemical resistance. Instead of an electrochemical model, a semi-empirical approach based on electrodes' polarization data is used to evaluate the electrochemical resistance of the battery (the resistance of electrode layers, electrolyte, and separator sheet). In addition, a finite-element numerical analysis along with supporting experimental data were employed to justify the assumptions in the analytical model. The numerical analysis employed in this study is initially introduced in Refs. 31, 32 and later adopted in Li-ion batteries by Kim et al.[33]

In the next sections, the problem of interest is defined by presenting the governing equations and the corresponding geometry, i.e., a unit cell (electrode assembly) of a prismatic Li-ion battery. Experimentation procedure and test results are presented for a sample large-scale battery and results of a finite-element analysis are discussed and validated through comparison with the experimental data. A section is devoted to theoretical analysis, in which a closed-form solution for potential and current density in current collectors is developed, and formulas for constriction/spreading and bulk resistance are presented. The analytical model is used to conduct a parametric study on how the dimensions of current collectors and design of the electrode tab effectuate the electrical conduction process and voltage drop. Furthermore, results of the theoretical analysis are validated against archival experimental data. In the last section, key observations and conclusions are presented.

Formulation of the Problem

Figure 1 shows a schematic of a unit cell in a prismatic lithium-ion battery, also called an electrode assembly, which includes several layers. For a better illustration the layers are shown separated in the figure, while they are compressed in the actual battery. Each unit cell includes a pair of current collectors, two pairs of electrode layers (positive and negative), and two separator sheets sandwiched between the electrodes. The electrodes, which accommodate active materials required in the battery chemistry, are laminated over current collector foils. The current collector foils in positive and negative electrodes are made from aluminum and copper, respectively. The separator sheet that acts as an inert membrane for Li^+ transport between the electrodes is a polymer. The electrodes and separators are porous and are soaked in a concentrated electrolyte liquid. The cell tabs are the current collector foils extending outside the electrode plates for the

[*]Electrochemical Society Active Member.
[**]Electrochemical Society Student Member.
[z]E-mail: ptaherib@sfu.ca
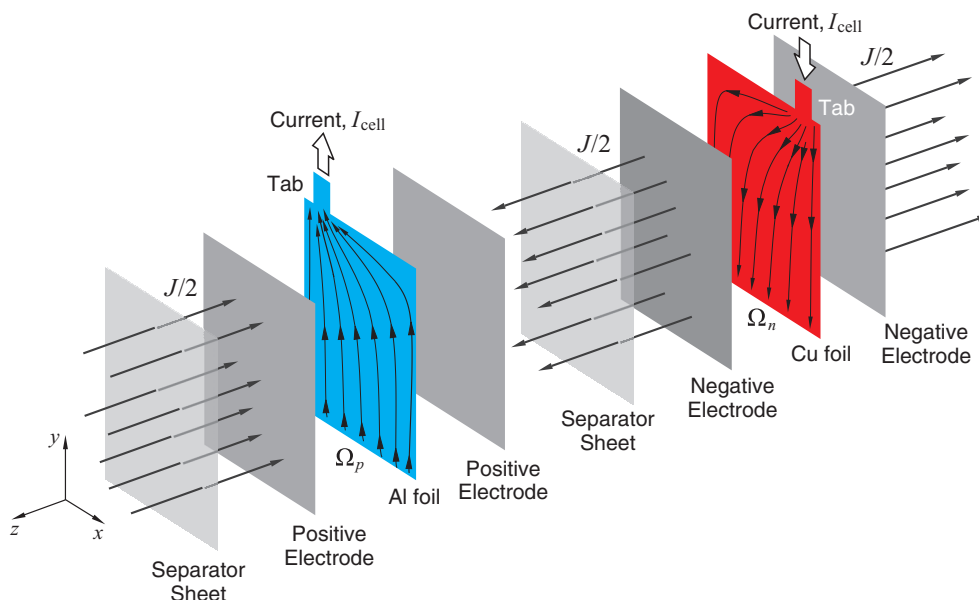
Figure 1. Schematic of a cell assembly in a prismatic lithium-ion battery is shown. The battery core is constructed by repeating the cell assembly. Different layers of the cell are separated for the sake of presentation. The arrows in z direction correspond reaction current, the transport of Li$^+$ from the negative electrode to the positive electrode during a discharge process. The arrows in x-y plane are current streamlines on current collectors.

purpose of electrical connection, and they are not covered by active materials.

Arrows in Fig. 1 present current streamlines during discharge processes; through-plane straight arrows correspond to the transport of lithium ions, Li$^+$, between the electrodes, and in-plane arrows in x-y plane represent the electrical current on current collectors. Because of the relatively high conductivity of the copper and aluminum current collectors as compared to the electrode materials, the in-plane current is assumed to be carried solely by the current collectors.[30,32] During a discharge process, as shown in Fig. 1, due to narrowing current passage at the tabs, electrical constriction and spreading respectively occur at the tabs of positive and negative electrodes. Concentration of streamlines at the vicinity of tabs results in a resistance, referred to as constriction/spreading resistance. If the tab width is equal to the electrode width, no current concentration occurs and the only resistance against the current is the bulk resistance.

A dimensional analysis can be performed to show that owing to the small thickness of the current collectors, compared to their dimensions in x and y directions, the distribution of current in the current collectors is two-dimensional in x-y plane.[30] Accordingly, the governing differential equation for the charge balance in each current collector reads

$$\sigma_j \frac{\partial^2 V_j}{\partial x^2} + \sigma_j \frac{\partial^2 V_j}{\partial y^2} + \frac{J \cdot \mathbf{n}}{\delta_j} = 0 \qquad (j = p, n) \qquad [1]$$

where x and y indicate the spatial coordinate system (m), σ is the electrical conductivity (S m^{-1}) of the current collector, V_j is the potential distribution (V) in the current collector, J is the through-plane current density distribution (A m^{-2}) due to electrochemical reactions between the electrodes on both sides, δ is the current collector thickness in z direction, and $\mathbf{n}$ is the unit normal vector on each current collector pointing inward. The subscript j corresponds to domains of the positive current collector Ω_p and the negative current collector Ω_n.

As depicted in Fig. 2, each current collector can be considered as a rectangular domain in x-y plane of width a and height c. The through-plane current enters (or exits) the domain through its surface in x-y plane, whereas the in-plane current is allowed to exit (or enter) the domain through the tab constriction of width b on the boundary at $y = c$.

is denoted by e. When $e = a/2$ the constriction is called "centric constriction" otherwise "eccentric constriction."

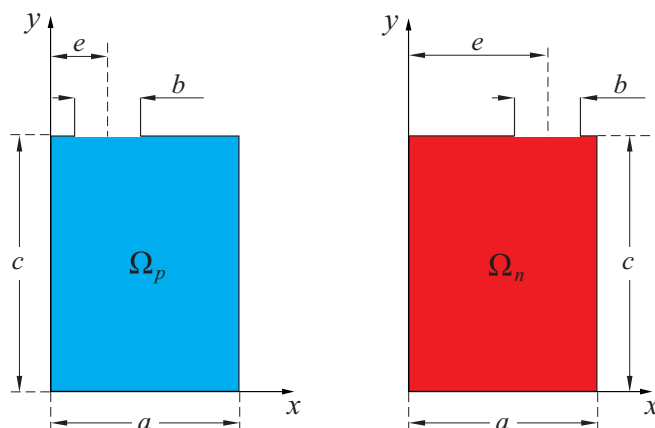With reference to Fig. 2, the relevant boundary conditions for Eq. 1 at the positive domain are

$$-\sigma_p \frac{\partial V_p}{\partial x} = 0 \quad \text{at} \quad x = 0 \qquad [2a]$$

$$-\sigma_p \frac{\partial V_p}{\partial x} = 0 \quad \text{at} \quad x = a \qquad [2b]$$

$$-\sigma_p \frac{\partial V_p}{\partial y} = 0 \quad \text{at} \quad y = 0 \qquad [2c]$$

$$-\sigma_p \frac{\partial V_p}{\partial y} = \frac{I_{cell}}{b \delta_p} \quad \text{at} \quad e - \frac{b}{2} < x < e + \frac{b}{2} \quad y = c \quad [2d]$$

$$-\sigma_p \frac{\partial V_p}{\partial y} = 0 \quad \text{at} \quad e + \frac{b}{2} < x < e - \frac{b}{2} \quad y = c \quad [2e]$$

Figure 2. Two-dimensional schematic of current collectors with a tab constriction of width b. The distance of the center of constriction from y axis is denoted by e.

Similarly, for the negative domain

$$-\sigma_n \frac{\partial V_n}{\partial x} = 0 \quad \text{at} \quad x = 0 \qquad \text{[3a]}$$

$$-\sigma_n \frac{\partial V_n}{\partial x} = 0 \quad \text{at} \quad x = a \qquad \text{[3b]}$$

$$-\sigma_n \frac{\partial V_n}{\partial y} = 0 \quad \text{at} \quad y = 0 \qquad \text{[3c]}$$

$$V_n = 0 \quad \text{at} \quad e - \frac{b}{2} < x < e + \frac{b}{2} \quad y = c \qquad \text{[3d]}$$

$$-\sigma_n \frac{\partial V_n}{\partial y} = 0 \quad \text{at} \quad e + \frac{b}{2} < x < e - \frac{b}{2} \quad y = c \qquad \text{[3e]}$$

The above boundary conditions imply that no current passes through boundaries of Ω_p and Ω_n except for the tab boundaries. In Eq. 2d, I_{cell} is the cell discharge current (A), and $b\,\delta_p$ is the cross-sectional area of the tab on the positive current collector. In Eq. 3d, voltage at the tab boundary of the negative current collector is set to zero in order to provide a reference for voltage distribution.[20]

The distribution of the through-plane current density is dictated by the local rate of electrochemical reactions in electrodes, which can be accurately described by detailed electrochemical models.[29,30]

In this study, a mathematical model[31,32] is employed to predict the time dependent behavior of the reaction current density during constant-current discharge processes in a sample Li-ion battery. The model uses experimentally determined polarization expressions to describe the overpotential between positive and negative electrodes.

Confirmed by experimental observations[32] and also electrochemical simulations,[28] at a fixed depth-of-discharge (DOD), the discharge voltage exhibits a linear dependency on current. Accordingly, a linear polarization expression can be assumed as[20,31,32]

$$J = Y_{\text{ec}} \left[(V_p - V_n) - V_{\text{oc}} \right] \qquad \text{[4]}$$

where J is related to the applied cell current I_{cell} (A) and the battery current I_{batt} (A) via

$$I_{\text{cell}} = \int_0^a \int_0^c J(x, y)\, dy\, dx \quad \text{and} \quad I_{\text{batt}} = I_{\text{cell}} N_{\text{elec}} \qquad \text{[5]}$$

Here, Y_{ec} (S m^{-2}) is the electrochemical conductance per unit area of the cell,[20] V_{oc} is the open-circuit (equilibrium) potential of the cell, and $V_p - V_n$ corresponds to the potential difference between a point on the positive current collector and the opposite point on the negative current collector. The number of electrode pairs [cf. Fig. 1] inside the battery is denoted by N_{elec}.

Both Y_{ec} and V_{oc} vary with respect to the DOD and their dependency can be approximated by the following polynomial fits

$$Y_{\text{ec}} = \sum_{l=0}^{L} \mathcal{C}_l \,(\text{DOD})^l \qquad \text{[6]}$$

$$V_{\text{oc}} = \sum_{m=0}^{M} \mathcal{D}_m \,(\text{DOD})^m \qquad \text{[7]}$$

where $\mathcal{C}_l$ and $\mathcal{D}_m$ are the constants to be determined from experiments.

We define DOD as the fraction of cell capacity Q_{cell} (Ah), released during a discharge process. Given an initial DOD at $t = 0$ and assuming 100% coulombic efficiency, DOD (in %) can be calculated in time t (s) as

$$\text{DOD}(t) = \text{DOD}(0) + \frac{1}{3600\, Q_{\text{cell}}} \int_0^t I_{\text{cell}}(t)\, dt \qquad \text{[8]}$$

where $Q_{\text{cell}} = Q_{\text{batt}} / N_{\text{elec}}$.

Once the boundary-value problem, i.e., Eqs. 1–3, is solved for a given DOD (or time), Ohm's law can be used to find the local in-plane current density on each current collector

$$i_{x,j} = -\sigma_j \frac{\partial V_j}{\partial x} \quad \text{and} \quad i_{y,j} = -\sigma_j \frac{\partial V_j}{\partial y} \qquad (j = p, n) \quad \text{[9]}$$

Experimental Study

We use a high-power prismatic Li-ion battery (AllCell Technologies, USA) as the experimental battery, with the nominal capacity of 75 Ah. With reference to Fig. 2, dimensions of current collectors in the battery and their electrical conductivity are given in Table I. The battery core (electrode stack) contains several pairs of positive and negative electrodes connected in parallel; nickel-cobalt-manganese cathode and graphite anode.

Constant-current discharge tests at C/2-rate (37.5 A), 1C-rate (75 A), 2C-rate (150 A), 4C-rate (300 A), and 5C-rate (375 A) were performed to measure the battery voltage V_{batt} during discharge processes. Each discharge test was performed with the battery un-insulated, lying flat on a perforated plastic rack in an environmental chamber (Envirotronics, ST-27) set at $25 \pm 0.5°$C. Before discharging, in order to establish a 100% state-of-charge, the battery was charged following the constant-current and constant-voltage (CC-CV) protocol, i.e., it was charged at 37.5 A until reaching 4.2 V, then held at 4.2 V until the charging current decreased to 3.75 A. The fully charged cell was then allowed to rest for an hour before a discharging test begins. Voltage data were recorded at a rate of 1 S s^{-1} over the duration of the tests. Sampled voltage values from measurements are shown in Fig. 3. The cutoff voltage for discharge tests was set to 2.7 V. To allow a discharged battery to return to ambient temperature and reach its electrochemical equilibrium, a minimum of four hours elapsed between the end of a discharge cycle and the beginning of the charge cycle.

Additionally, open-circuit potential of the battery was experimentally determined by discharging the cell at a C/20-rate (3.75 A) at 25°C inside the environmental chamber. All discharge tests were performed with a multi-channel power cycler (Arbin Instruments, BT-2000).

As shown in Eqs. 6 and 7, Y_{ec} and V_{oc} depend on DOD. Their values at various DOD are estimated from measured data of the battery voltage versus current.[32] As shown in Fig. 4, at a constant DOD, the actual variation of voltage versus current (symbols in Fig. 4) can be approximated by a linear function (lines in Fig. 4), where Y_{ec} is the inverse of the line slope and V_{oc} is the intercept.

Values for V_{oc} and Y_{ec} at different DOD, obtained from measurements and above-mentioned procedure, are plotted in Fig. 5. In order to check the accuracy of our approximation, experimentally obtained open-circuit voltage of the battery is compared to the approximated values in Fig. 5(a); the comparison shows a satisfactory agreement. Solid lines in Fig. 5 represent seventh-order polynomial fits to the

Table I. The dimensions and electrical conductivity of current collectors in positive and negative electrodes of the battery.

	a (m)	b (m)	c (m)	e (m)	Thickness δ (m)	Electrical conductivity σ (S m^{-1})
Positive	248×10^{-3}	80×10^{-3}	229×10^{-3}	60×10^{-3}	$20 \times 10^{-6*}$	37.8×10^6
Negative	248×10^{-3}	80×10^{-3}	229×10^{-3}	188×10^{-3}	$14 \times 10^{-6*}$	59.6×10^6

*From Ref. 17.
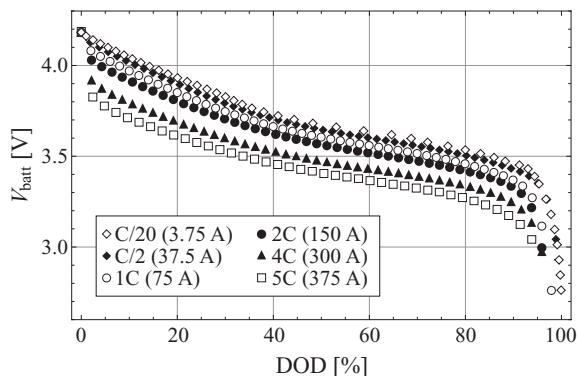
Figure 3. Measured voltage response of the battery during constant-current discharge processes at different discharge rates at an environmental temperature of 25°C.

approximated values, i.e., $L = M = 7$ in Eqs. 6 and 7. The coefficients $\mathcal{C}_l$ and $\mathcal{D}_m$ for these polynomials are listed in Appendix A.

Numerical Analysis

Equation 1 along with boundary conditions 2 and 3 can be solved numerically, because the governing Poisson equations for positive and negative domains are non-homogeneous and highly coupled via their source terms.

In the present work, a finite element PDE solver, COMSOL MULTIPHYSICS (Version 4.3a), is used to simultaneously solve system 1–3 over two separated domains, Ω_p and Ω_n, and obtain the voltage and current density distributions at different DOD values.

Once the voltage distribution on current collectors is obtained numerically, the battery voltage V_{batt} can be calculated as

$$V_{batt} = \frac{1}{b} \int_{e-\frac{b}{2}}^{e+\frac{b}{2}} V_p(x, c) \, dx \qquad [10]$$

where b is the width of the tab.

In Fig. 6, voltage response of the battery at different discharge rates is calculated from numerical simulations with Eq. 10, and is compared to measured voltage values, i.e., data in Fig. 3. The comparison shows an excellent agreement between the calculated an measured volt-
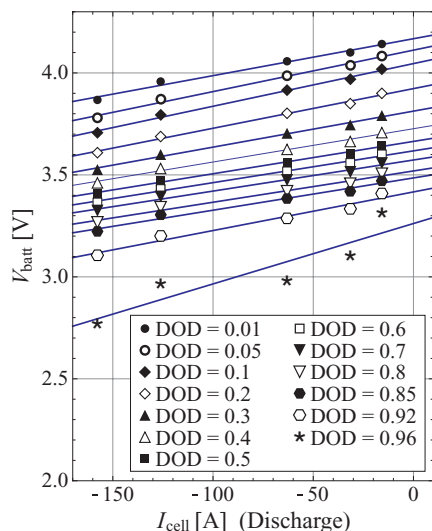
Figure 4. (Color online) Linear dependency of voltage and current at constant values of depth-of-discharge (DOD) is shown.
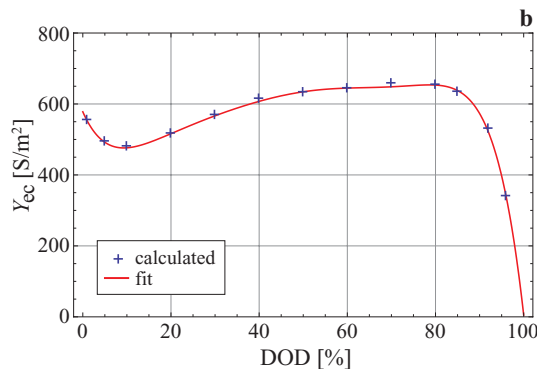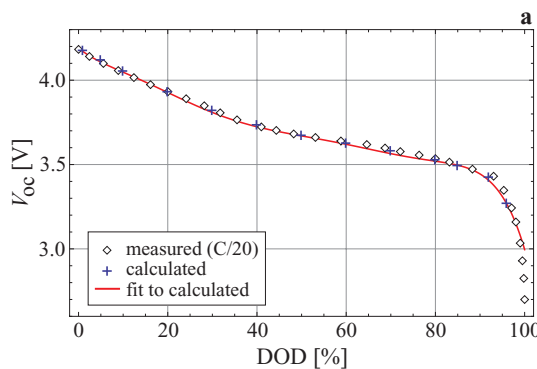

Figure 5. (Color online) Dependency of open-circuit potential V_{oc} and electrochemical conductance Y_{ec} on depth-of-discharge (DOD).

age of the battery, even at the nonlinear portion of discharge curves. Note that since electrodes inside the battery are connected in parallel, $V_{batt} = V_{cell}$.

In Figs. 7 and 8, numerical solutions to the governing equations [cf. Eqs. 1–4] are shown for the sample battery.

Plots (a) and (b) in Fig. 7 respectively correspond to voltage distribution on the positive and negative current collectors at $t = 600$ s (DOD = 16%) during a 1C-rate discharge process. Similarly, plots (c) and (d) correspond to the same data at $t = 3480$ s (DOD = 96%) for a 1C-rate discharge. Current collector tabs are indicated by gray rectangles on the top edge of the domain. In the plots, the magnitude of voltage is shown with colors, black lines are equipotential lines, and white lines are current streamlines. As expected, equipotential lines and streamlines are perpendicular all over the domain. Convergence and divergence of current streamlines at the tabs represent the electrical constriction and spreading resistances.
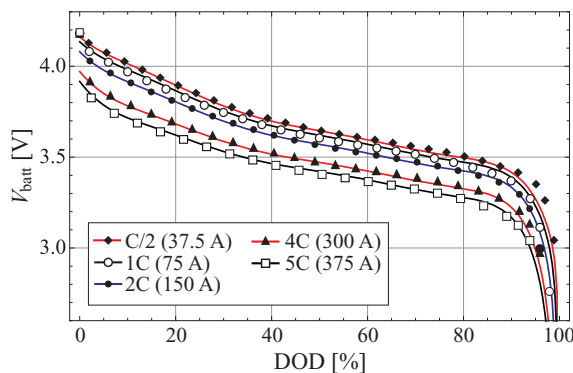
Figure 6. (Color online) Variation of battery voltage versus depth-of-discharge (DOD) for different discharge currents are shown. Symbols correspond to measured values and lines represent the calculated values.
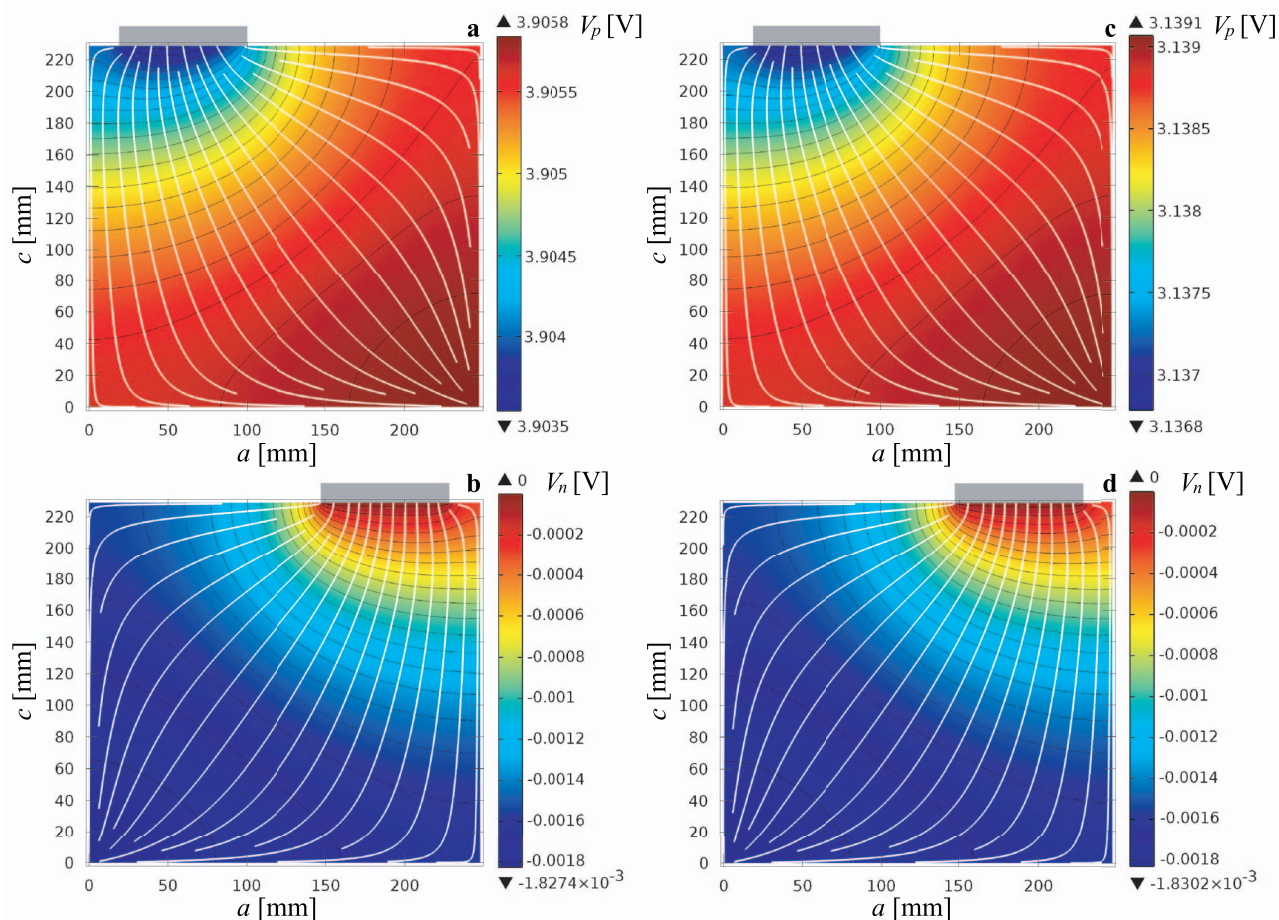
Figure 7. (Color online) The voltage distributions on current collectors are shown for a 1C-rate discharge. Plots (a) and (b) respectively correspond to voltage distribution on the positive current collector V_p and voltage distribution on the negative current collector V_n at DOD = 16%. Plots (c) and (d) present to the same data at DOD = 96%. Voltage magnitude is shown with contours (color maps with equipotential black lines) and current streamlines are depicted with white lines. Current collector tabs are indicated by gray rectangles on the top edge of the domain.

Plot (a) in Fig. 8, shows the distribution of through-plane current density, J, between the electrodes at $t = 600\,\text{s}$ (DOD = 16%) during a 1C-rate discharge process. Plot (b), shows the same data at $t = 3480\,\text{s}$ (DOD = 96%) for a 1C-rate discharge.

The results in Fig. 7 show that the distribution pattern for voltage and in-plane current density remain the same during the whole constant-current discharge process, while the magnitude of voltage decreases with DOD [cf. Fig. 6]. Quite differently, as depicted in
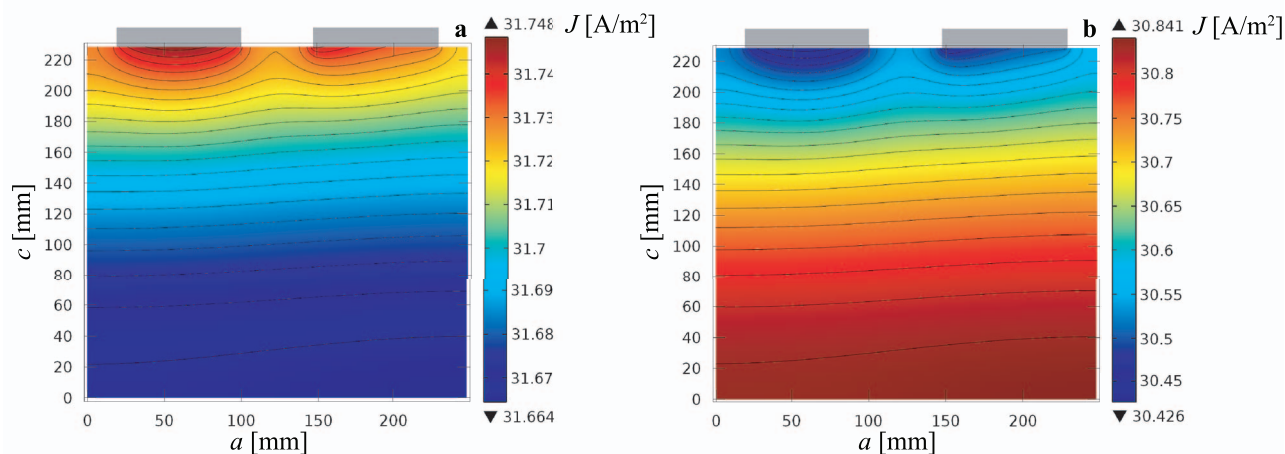
Figure 8. (Color online) The reaction current density between the current collectors are shown for a 1C-rate discharge at: a) DOD = 16%, and b) DOD = 96%.
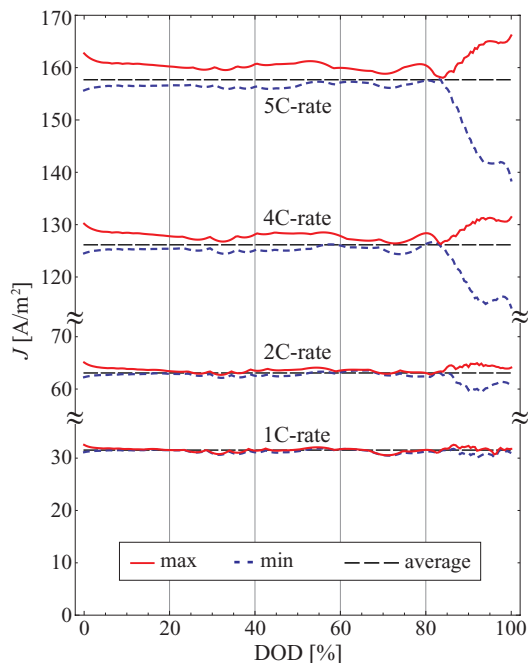
Figure 9. (Color online) Minimum, maximum, and averaged values of reaction current with respect to DOD are shown for different discharge rates.
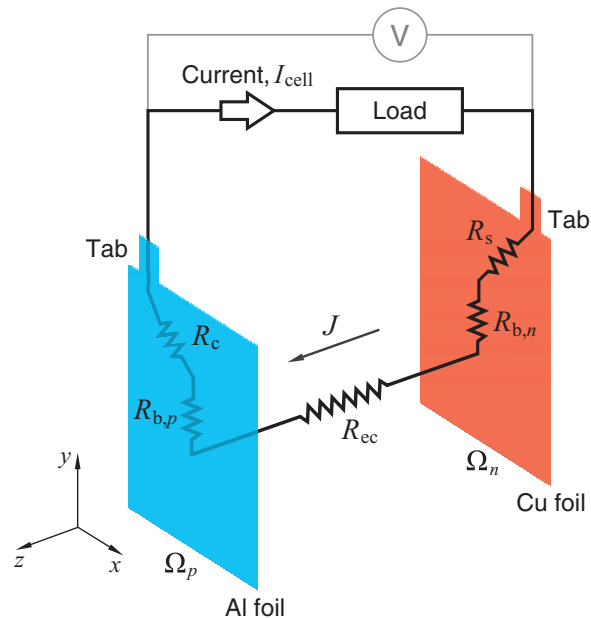

Figure 10. (Color online) Internal resistances of a cell are schematically shown for an arbitrary current path. Spreading and constriction resistances, shown by R_s and R_c, occur at the vicinity of tabs. The bulk resistances in current collectors are $R_{b,j}$, and R_{ec} is the electrochemical resistance.

Fig. 8, the distribution pattern for through-plane (reaction) current density, J, changes drastically. Our simulations show that for DOD $\lesssim 5\%$ the through-plane current density is higher at the vicinity of tabs. At $5 \lesssim$ DOD $\lesssim 85\%$ the distribution of reaction current becomes more uniform, but still remains slightly higher near the tabs. However, near the end of discharge, i.e., for DOD $\gtrsim 85\%$, when active materials are depleted at the top side of the electrodes near the tabs, the through-plane reaction current is forced away from the tabs toward the bottom of current collectors where active materials are less utilized. We observed the same behavior at all discharge currents (not shown here), nonetheless, such non-uniformities in reaction current become stronger at higher discharge rates.

In order to investigate uniformity of the through-plane current density at different discharge rates, minimum and maximum values of J with respect to DOD are obtained numerically and plotted in Fig. 9. Solid lines in Fig. 9 represent the maximum values, dotted lines denote its minimum values, and the averaged value, $\bar{J} = I_{cell}/(a\,c)$, is depicted by dashed lines. The plots reveal that for DOD $< 85\%$ variations of J are not drastic, nevertheless, for DOD $> 85\%$ such variations become more pronounced, particularly at high discharge currents.

As given in Eq. 4, uniformity of the through-plane current density strongly depends on variations of Y_{ec} and V_{oc} with respect to DOD; indeed, our investigations show that variations of V_{oc} are dominant. The considered nickel-cobalt-manganese/graphite battery exhibits sharp variations in Y_{ec} and V_{oc} for DOD $> 85\%$; however, at low temperatures or for specific chemistries (iron-phosphate/graphite cells), variations of Y_{ec} and V_{oc} can be significant at small DOD as well owing to activation effects (mass transfer resistance). Accordingly, the DOD limit for a uniform reaction current may vary for different cases, and so the applicability of this model.

Ohmic Resistance Analysis

The voltage drop between battery tabs with respect to the open-circuit potential, $V_{oc} - V_{batt}$, is the result of internal resistances which can be split into: *i)* spreading resistance R_s and constriction resistances R_c at the current collector tabs, *ii)* electrical resistances $R_{b,j}$ of current collectors (bulk resistance), and *iii)* the electrochemical resistance R_{ec}; the inverse of the electrochemical conductance Y_{ec}. For an arbitrary current path, these resistances are schematically shown in Fig. 10.

In this section, we develop a closed-form analytical model to evaluate the contribution of ohmic resistances, i.e., spreading/constriction and bulk resistances, to the battery voltage drop. For this, we shall first set $R_{ec} = 0$ and solve Eqs. 1–3 to find the voltage difference between the tabs. Nonetheless, in order to properly define this problem, a through-plane current density must be assumed.

Results from the numerical analysis confirm that the reaction current density, J, is not uniform; however, its local variations are not drastic, particularly for DOD $< 85\%$; see Fig. 9. Accordingly, a uniform reaction current density, $\bar{J}$, is superimposed in our analysis which allows to develop a theoretical model for ohmic resistances in the current collectors. Note that uniformity of reaction current density is a desired feature for Li-ion batteries, as it means that active material are evenly utilized and battery degradation rate is minimized.

Analytical model for voltage and current density distributions.— We define a new variable to transform the governing Poisson equation, Eq. 1, and the corresponding boundary conditions, Eqs. 2 and 3, into a Laplace equation, for which an analytical solution is accessible with the method of separation of variables.

Let's introduce a new variable ξ, that relates V to $\bar{J}$ via

$$V_j(x, y) = \xi_j(x, y) - \frac{1}{2}\frac{\bar{J} \cdot \mathbf{n}}{\delta_j \sigma_j} y^2 \qquad (j = p, n) \qquad [11]$$

where $\bar{J} = I_{cell}/(a\,c)$ is the averaged through-plane current density.

Substituting $V_j(x, y)$ from Eq. 11 into Eq. 1 and boundary conditions 2 and 3 yields the following homogeneous equation

$$\frac{\partial^2 \xi_j}{\partial x^2} + \frac{\partial^2 \xi_j}{\partial y^2} = 0 \qquad (j = p, n) \qquad [12]$$

with the transformed boundary conditions for the positive current collector

$$\frac{\partial \xi_p}{\partial x} = 0 \quad \text{at} \quad x = 0 \qquad [13a]$$

$$\frac{\partial \xi_p}{\partial x} = 0 \quad \text{at} \quad x = a \qquad [13b]$$

$$\frac{\partial \xi_p}{\partial y} = 0 \quad \text{at} \quad y = 0 \qquad [13c]$$

$$\frac{\partial \xi_p}{\partial y} = \frac{\bar{J} c}{\delta_p \sigma_p} \left(1 - \frac{a}{b}\right) \quad \text{at} \quad e - \frac{b}{2} < x < e + \frac{b}{2} \quad y = c \qquad [13d]$$

$$\frac{\partial \xi_p}{\partial y} = \frac{\bar{J} c}{\delta_p \sigma_p} \quad \text{at} \quad e + \frac{b}{2} < x < e - \frac{b}{2} \quad y = c \qquad [13e]$$

and for the negative current collector

$$\frac{\partial \xi_n}{\partial x} = 0 \quad \text{at} \quad x = 0 \qquad [14a]$$

$$\frac{\partial \xi_n}{\partial x} = 0 \quad \text{at} \quad x = a \qquad [14b]$$

$$\frac{\partial \xi_n}{\partial y} = 0 \quad \text{at} \quad y = 0 \qquad [14c]$$

$$\frac{\partial \xi_n}{\partial y} = -\frac{\bar{J} c}{\delta_n \sigma_n} \left(1 - \frac{a}{b}\right) \quad \text{at} \quad e - \frac{b}{2} < x < e + \frac{b}{2} \quad y = c \qquad [14d]$$

$$\frac{\partial \xi_n}{\partial y} = -\frac{\bar{J} c}{\delta_n \sigma_n} \quad \text{at} \quad e + \frac{b}{2} < x < e - \frac{b}{2} \quad y = c \qquad [14e]$$

Note that in derivation of Eq. 13d, the cell discharge current I_{cell} is replaced with $a c \bar{J}$. Also, in Eq. 14d an equivalent second-type (Neumann) boundary condition is introduced instead of the original first-type (Dirichlet) boundary condition, because the method of separation of variables cannot be applied on a Laplace equation [cf. Eq. 12] with a first-order boundary condition.[34] Indeed, in the transformed system 12–14, the through-plane current density $\bar{J}$ is eliminated from the source term of the original Poisson equation [cf. Eq. 1] and its effect are reflected on the transformed boundary conditions.

Since geometries of the domains are similar (see Fig. 2) and the governing equations are the same, it suffices to discuss the details of the analytical solution for one of the domains—the same approach can be applied to the other domain as well. Here, we consider the positive domain and omit the subscript "p" in the following formulas for the sake of better readability.

Using the method of separation of variables, the general solution for Eq. 12 can be obtained as

$$\xi(x, y) = \sum_{k=1}^{\infty} A_k \cos(\alpha_k x) \cosh(\alpha_k y) \qquad [15]$$

in which the summation is taken over all discrete spectrum of eigenvalues $\alpha_k = k\pi/a$. The terms $\cos(\alpha_k x)$ and $\cosh(\alpha_k y)$ are the eigenfunctions, and A_k is the coefficient to be determined from boundary

conditions at $y = c$, i.e.

$$\sum_{k=1}^{\infty} A_k \alpha_k \cos(\alpha_k x) \sinh(\alpha_k c)$$
$$= \begin{cases} \dfrac{\bar{J} c}{\delta \sigma} \left(1 - \dfrac{a}{b}\right) & \text{at} \quad e - \dfrac{b}{2} < x < e + \dfrac{b}{2} \\ \dfrac{\bar{J} c}{\delta \sigma} & \text{at} \quad e + \dfrac{b}{2} < x < e - \dfrac{b}{2} \end{cases} \qquad [16]$$

The unknown coefficient A_k must be obtained from the orthogonality condition for eigenfunctions[34,35]

$$\int A_k \alpha_k \cos(\alpha_k x) \cos(\alpha_l x) \sinh(\alpha_k c) \, dx = 0 \quad \text{for} \quad k \neq l \qquad [17]$$

Thus, multiplying both sides of Eq. 16 with $\cos(\alpha_l x)$ and subsequent integrating yields the following relation for $k = l$

$$\int_0^a A_k \alpha_k \cos^2(\alpha_k x) \sinh(\alpha_k c) \, dx$$
$$= \frac{\bar{J} c}{\delta \sigma} \left[\int_0^{e-\frac{b}{2}} \cos(\alpha_k x) \, dx + \left(1 - \frac{a}{b}\right) \int_{e-\frac{b}{2}}^{e+\frac{b}{2}} \cos(\alpha_k x) \, dx \right.$$
$$\left. + \int_{e+\frac{b}{2}}^{a} \cos(\alpha_k x) \, dx \right] \qquad [18]$$

from which A_k is evaluated as

$$A_k = \frac{4 \bar{J} c \, [b \sin(\alpha_k a) - 2a \cos(\alpha_k e) \sin(\alpha_k b/2)]}{\delta \sigma b \, \alpha_k \sinh(\alpha_k c) \, [2\alpha_k a + \sin(2\alpha_k a)]} \qquad [19]$$

Finally, the solution for potential $V(x, y)$ follows from Eq. 11

$$V(x, y) = \sum_{k=1}^{\infty} A_k \cos(\alpha_k x) \cosh(\alpha_k y) - \frac{1}{2} \frac{\bar{J}}{\delta \sigma} y^2 \qquad [20]$$

with A_n as given in Eq. 19. Once the voltage distribution is known, the in-plane current distribution can be obtained from Eq. 9.

The solution for $V(x, y)$ in Eq. 20 is the superposition of a one-dimensional potential distribution, $-\bar{J} y^2/(2\delta\sigma)$, and a two-dimensional potential distribution, $\sum A_k \cos(\alpha_k x) \cosh(\alpha_k y)$. It is apparent that where no constriction exists, i.e., $b = a$ and $e = a/2$, the two-dimensional part of the solution vanishes, since $A_k = 0$.

Constriction resistance model.— The resistance that results from constriction of current at the positive current collector tab can be defined as

$$R_c = \frac{|\bar{V}_c - V_{nc}|}{\bar{J} \, a \, c} \qquad [21]$$

where $\bar{V}_c$ is the averaged potential along the constriction width b and V_{nc} is the potential at $y = c$ when there is no constriction ($b = a$ and $e = a/2$). The units for R_c is ohm (Ω). In order to find $\bar{V}_c - V_{nc}$ one

can use the solution in 20 to obtain

$$\bar{V}_c - V_{nc} = \frac{1}{b} \int_{e-\frac{b}{2}}^{e+\frac{b}{2}} V(x,c)\,dx + \frac{1}{2}\frac{\bar{J}c^2}{\delta\sigma}$$

$$= \frac{8\bar{J}c}{b^2\delta\sigma} \sum_{k=1}^{\infty} \frac{\cos(\alpha_k e)\coth(\alpha_k c)\sin(\alpha_k b/2)\,[b\sin(\alpha_k a) - 2a\cos(\alpha_k e)\sin(\alpha_k b/2)]}{\alpha_k^2\,[2\alpha_k a + \sin(2\alpha_k a)]} \qquad [22]$$

Replacing Eq. 22 in 21, yields a closed-form expression for constriction resistance, which is a function of geometrical parameters a, b, c, e, and electrical conductivity $\sigma >$

$$R_c = \frac{8}{a\,b^2\delta\sigma} \sum_{k=1}^{\infty} \frac{\cos(\alpha_k e)\coth(\alpha_k c)\sin(\alpha_k b/2)\,[b\sin(\alpha_k a) - 2a\cos(\alpha_k e)\sin(\alpha_k b/2)]}{\alpha_k^2\,[2\alpha_k a + \sin(2\alpha_k a)]} \qquad [23]$$

For the sake of comparison with experimental data, following Refs. 36 and 37, we define Y_c as the constriction conductance per unit area (the term constriction conductance, when used, represents the reciprocal value of the constriction resistance)

$$Y_c = \frac{1}{a\delta R_c} \qquad [24]$$

Equation 24 can be rewritten in the following dimensionless form

$$\frac{1}{\Psi_c} = -\frac{8}{\varepsilon_b^2\pi^3} \sum_{k=1}^{\infty} \frac{\sin^2(k\pi\varepsilon_b/2)\cos^2(k\pi\varepsilon_e)\coth(k\pi\varepsilon_c)}{k^3} \qquad [25]$$

in which the eigenvalues $\alpha_k = k\pi/a$ are introduced. The dimensionless conductance number Ψ_c and three aspect ratios are

$$\Psi_c = \frac{a\,Y_c}{\sigma}, \qquad \varepsilon_b = \frac{b}{a}, \qquad \varepsilon_c = \frac{c}{a}, \qquad \varepsilon_e = \frac{e}{a} \qquad [26]$$

For convenience, we name ε_b, ε_c, and ε_e as constriction number, domain aspect ratio, and eccentricity number, respectively. Based on Fig. 2, variation ranges for aspect ratios are $0 < \varepsilon_b < 1$, $\varepsilon_c > 0$, and $\varepsilon_b/2 < \varepsilon_e < 1 - \varepsilon_b/2$.

Bulk resistance.— In Eq. 21, if we set $\bar{V}_c = 0$, it gives the bulk resistance of the current collector. Additionally, from the analytical solution 20 we know that $V_{nc} = -\bar{J}y^2/(2\delta\sigma)$, hence, the formula for bulk resistance becomes

$$R_b = \frac{c}{2a\delta\sigma} = \frac{\varepsilon_c}{2\delta\sigma} \qquad [27]$$

Equation 27 confirms that thicker current collectors with small domain aspect ratios and high electronic conductivities are preferred to reduce the bulk resistance.

Results and Discussion

In this section a parametric study is performed to describe the effects of current collectors configuration on constriction and spreading resistances inside the battery. Furthermore, the results are validated against experimental data from Refs. 36, 38, and 39.

Constriction conductance, as formulated in Eq. 25, turns out to be independent of how the current $\bar{J}$ is supplied into the domain. This makes it possible to verify the present model against empirical data obtained for the cases in which the current was supplied at the boundaries of the domain;[36,38,39] see Ref. 36 for details on experiment setup.

In Fig. 11, results of the constriction model for a centric tab ($\varepsilon_e = 1/2$) are compared to experimental data. The plot shows the variation of conductance number Ψ_c with respect to constriction number ε_b for different values of domain aspect ratio ε_c. The experimental data from Refs. 36, and 38 are shown with symbols (circles and

diamonds), and are obtained for long strips of thin resistive papers with large domain aspect ratios; $\varepsilon_c \gg 1$. The results of our model remain invariant for $\varepsilon_c > 1$, however, as expected, for smaller domain aspect rations the conductance number decreases, due to increase in constriction resistance. To test the accuracy of the model, the series solution for Ψ_c is plotted by 200 eigenvalues ($k = 200$), but even for a small number of eigenvalues, i.e., $k < 7$, the model fairly predicts the measurements, except for very small constrictions, $\varepsilon_b < 0.1$.

It is worth mentioning that at the limits, where $\varepsilon_b \to 0$ and $\varepsilon_b \to 1$, all curves in Fig. 11 converge to minimum and maximum values of the conductance number.

To investigate the effects of eccentricity on constriction conductance, variation of normalized conductance number Ψ_c/Ψ_0 with respect to ε_b and ε_e is shown in Fig. 12(a), where Ψ_0 is the conductance number for a given constriction number ε_b, with no eccentricity, $\varepsilon_e = 1/2$. In Figs. 12(b)–(d), for fixed values of ε_b, variation of Ψ_c/Ψ_0 with respect to ε_e is compared to experimental data.[36,39] The results confirm that constriction conductance decreases when eccentricity increases. The comparisons also show a precise prediction of the proposed model. Since in Refs. 36 and 39, eccentricity is defined with respect to the centerline of the domain width, the measured data are reported only for half of the domain width, owing to symmetry about the centerline.

For the considered battery, according to Eq. 23, spreading resistance at the negative current collector is 1.57 mΩ and constriction resistance at the positive current collector is 1.74 mΩ. This minor difference is a result of different thicknesses and electrical conductivities of copper and aluminum foils; see Table I. Furthermore, from Eq. 27, bulk resistances in negative and positive current collectors are calculated as 0.55 mΩ and 0.61 mΩ, respectively. This reveals that constriction/spreading resistance in current collectors has a larger contribution to ohmic losses compared to their bulk resistance.

In Fig. 13, variation of the electrochemical resistance with respect to DOD, obtained from data in Fig. 5(b), is plotted.
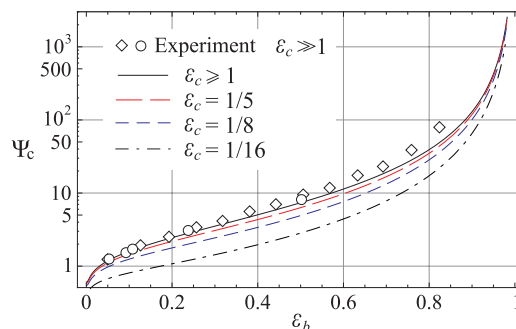
Figure 11. (Color online) For a centric tab, effects of constriction number ε_b and domain aspect ratio ε_c on conductance number Ψ_c is shown. As ε_c decreases constriction resistance increases (the conductance number decreases). The symbols are experimental data from Refs. 36 and 38 for $\varepsilon_c \gg 1$.
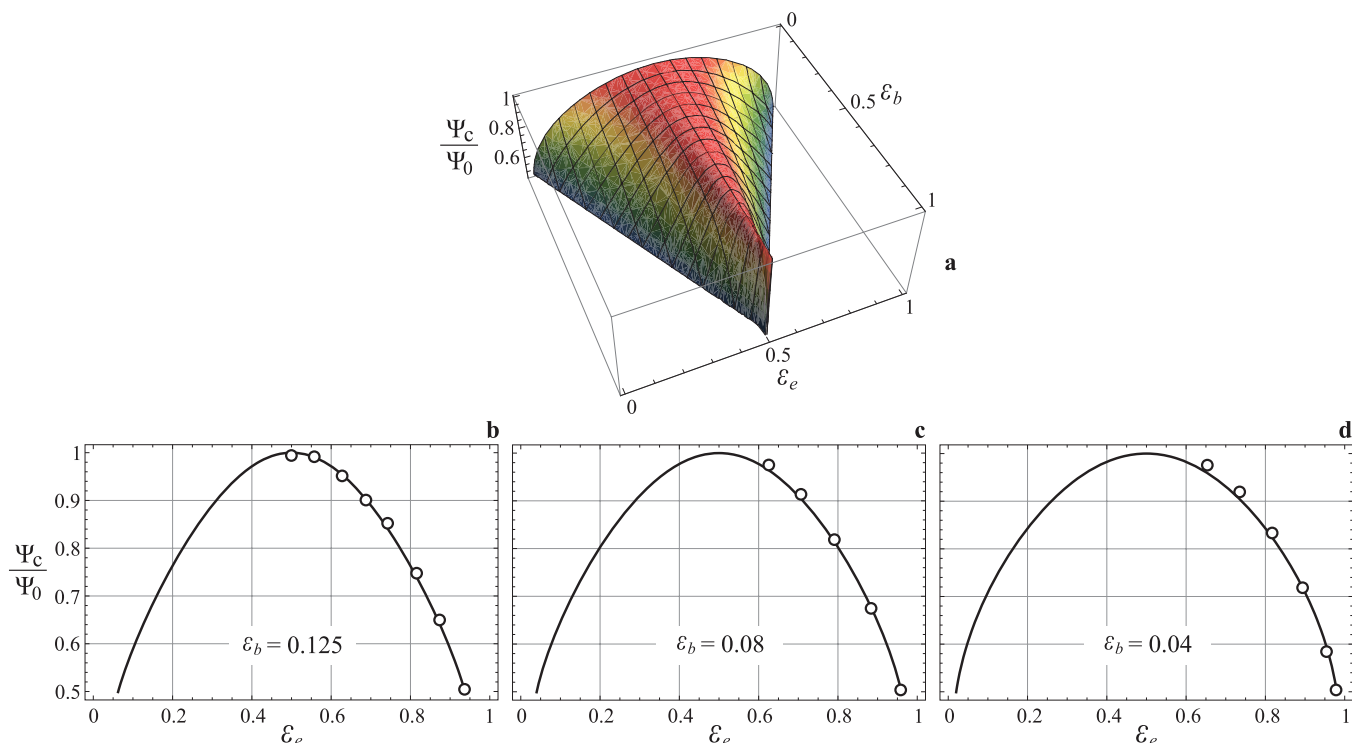
Figure 12. (Color online) a) Variation of normalized conductance number Ψ_c / Ψ_0 with respect to constriction number ε_b and eccentricity number ε_c is shown. b–d) for fixed values of ε_b model predictions for Ψ_c / Ψ_0 are compered to experimental data from Ref. 36 in plot (b), and experimental data from Ref. 39 in plots (c) and (d).
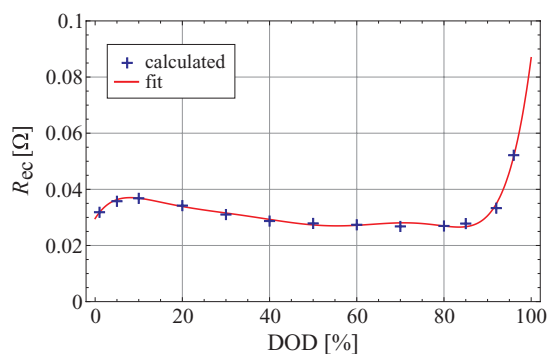
Figure 13. (Color online) Dependency of electrochemical resistance R_{ec} on depth-of-discharge (DOD).

Comparison between the magnitudes of different resistances shows that when DOD $<$ 85%, contribution of the constriction/spreading resistance to the total resistance is about 10%, whereas only about 3% of the total resistance is the result of bulk resistances.

Conclusions

In this study, a new mathematical procedure was developed that accurately predicts the contributions of bulk and spreading/constriction resistances to internal losses of lithium-ion batteries with planar tabbed configuration. The following steps were taken to develop and validate the present model:

• a large-scale lithium-ion battery (75 Ah) was characterized experimentally to obtain its polarization expressions,
• time dependence behavior of the battery during glavanostatic discharge processes was simulated numerically to investigate distributions of the reaction current, the voltage, and the secondary current in the electrode assembly,

• based on the assumption that the governing equations for two fields (positive and negative electrodes) can be decoupled, an analytical model was proposed to approximate ohmic resistances is current collectors of the battery. The assumption required for development of the analytical model was justified by an independent full numerical simulation of the problem.
• a compact series-form solution for electrical constriction and spreading resistances in current collectors of the battery was obtained and validated through comparisons with experimental data available in the literature.

We emphasize that in developing the present analytical model, it was assumed that the reaction current density is uniformly distributed between electrodes, which is a valid assumption for DOD $<$ 85% confirmed by numerical simulations.

The constriction/spreading resistance model was used to conduct a parametric study on the effects of current collectors configuration in ohmic losses. For the considered battery, the model estimated the contributions of spreading/constriction resistance and bulk resistance to be about 10% and 3% of the total resistance, respectively. Since resistance values for the experimental battery are fairly small, one may conclude that the battery includes well-designed electrodes. However, for other batteries, contributions of spreading/constriction and bulk resistances may be much higher.

The results confirms that constrictions/spreading resistance increase as:

• domain aspect ratio (ratio of length to width) decreases,
• width of the tab decreases,
• tab eccentricity increases,
• electrical conductivity decreases,

To conclude, it is important to emphasis on the importance of constriction/spreading resistance on the thermal behavior of Li-ion batteries. Experimental observations confirm that during charge and discharge of a Li-ion battery, temperature at the vicinity of the tabs

is higher compared to other parts of the battery, which is the direct result of increased current density at the tab constriction. Accordingly, the analysis presented in this study provides guideline for sizing current collectors and locating tabs in batteries with stacked electrode designs. Furthermore, this simple model may be preferred to three-dimensional models for optimizing the thermal design of electrodes in such batteries.

List of Symbols

a	width of current collector (m)
b	width of tab (m)
c	height of current collector (m)
$\mathcal{C}_l$	interpolation coefficients for Y_{ec}
$\mathcal{D}_m$	interpolation coefficients for V_{oc}
e	distance of tab center from y-axis (m)
i_x	horizontal component of current density on current collector (A m^{-2})
i_y	vertical component of current density on current collector (A m^{-2})
I	applied current (A)
J	reaction current density (A m^{-2})
$\bar{J}$	averaged reaction current density (A m^{-2})
$\mathbf{n}$	unit normal vector on current collector, pointing inward
N_{elec}	number of cells (electrode pairs) in battery
Q	capacity (Ah)
R_{ec}	electrochemical resistance (Ω)
R_c	constriction resistance in current collector tab (Ω)
R_s	spreading resistance in current collector tab (Ω)
R_b	bulk resistance in current collector (Ω)
t	time (s)
V	potential (V)
V_{oc}	open-circuit potential (V)
$\bar{V}_c$	averaged potential on constriction tab (V)
V_{nc}	potential on full width (no constriction) tab (V)
x	horizontal position (m)
y	vertical position (m)
Y_{ec}	electrochemical conductance per unit area (S m^{-2})
Y_c	constriction conductance per unit area (S m^{-2})
DOD	depth-of-discharge
Li-ion	lithium-ion

Greek

α_k	kth eigenvalue
δ	thickness of current collector (m)
ε_b	constriction number
ε_c	domain aspect ratio
ε_e	eccentricity number
ξ	voltage transformation variable (V)
σ	electrical conductivity (S m^{-1})
Ψ_c	conductance number
Ψ_0	conductance number for a centric tab

Superscript

batt	related to battery
cell	related to cell (electrode pair)
n	related to the negative domain
p	related to the positive domain

Appendix A. Polarization Coefficients for the Sample Battery

Table A1. Fitting coefficients for Y_{ec} and V_{oc}.

$\mathcal{C}_l$	Value (S m^{-2})	$\mathcal{D}_m$	Value (V)
$\mathcal{C}_0$	577.9476735438233	$\mathcal{D}_0$	4.1900257826837235
$\mathcal{C}_1$	-2826.608057060516	$\mathcal{D}_1$	-2.150679695021936
$\mathcal{C}_2$	27385.55389431569	$\mathcal{D}_2$	13.825682722952642
$\mathcal{C}_3$	-118117.8766617597	$\mathcal{D}_3$	-90.88309166466188
$\mathcal{C}_4$	293129.8099605549	$\mathcal{D}_4$	295.80459188445144
$\mathcal{C}_5$	-423319.09859033383	$\mathcal{D}_5$	-486.49943290364536
$\mathcal{C}_6$	326731.85507288034	$\mathcal{D}_6$	393.60780370820726
$\mathcal{C}_7$	-103556.43253825707	$\mathcal{D}_7$	-124.89928194000181

References

1. S. Szpak, C. J. Gabriel, and J. R. Driscoll, *Electrochim. Acta*, **32**, 239 (1987).
2. T. M. Bandhauer, S. Garimella, and T. F. Fuller, *J. Electrochem. Soc.*, **158**, R1 (2011).
3. J. Lee, K. W. Choi, N. P. Yao, and C. C. Christianson, *J. Electrochem. Soc.*, **133**, 1286 (1986).
4. Y. Chen, *J. Electrochem. Soc.*, **140**, 1833 (1993).
5. Y. Chen and J. W. Evans, *J. Electrochem. Soc.*, **141**, 2947 (1994).
6. C. R. Pals and J. Newman, *J. Electrochem. Soc.*, **142**, 3274 (1995).
7. Y. Chen and J. W. Evans, *J. Electrochem. Soc.*, **143**, 2708 (1996).
8. L. Song and J. W. Evans, *J. Electrochem. Soc.*, **145**, 2327 (1998).
9. S. Al-Hallaj and J. R. Selman, *J. Power Sources*, **110**, 341 (2002).
10. S. C. Chen, C. C. Wan, and Y. Y. Wang, *J. Power Sources*, **140**, 111 (2005).
11. K. Smith and C.-Y. Wang, *J. Power Sources*, **160**, 662 (2006).
12. G.-H. Kim, A. Pesaran, and R. Spotnitz, *J. Power Sources*, **170**, 476 (2007).
13. R. Sabbah, R. Kizilel, J. R. Selman, and S. Al-Hallaj, *J. Power Sources*, **182**, 630 (2008).
14. P. Taheri, M. Yazdanpour, and M. Bahrami, *J. Power Sources*, **243**, 280 (2013).
15. D. Bernardi, E. Pawlikowski, and J. Newman, *J. Electrochem. Soc.*, **132**, 5 (1985).
16. L. Rao and J. Newman, *J. Electrochem. Soc.*, **144**, 2697 (1997).
17. Y. Ye, Y. Shi, N. Cai, J. Lee, and X. He, *J. Power Sources*, **199**, 227 (2012).
18. G. G. Botte, B. A. Johnson, and R. E. White, *J. Electrochem. Soc.*, **146**, 914 (1999).
19. S.-H. Ng, H. La Mantia, and F. Novák, *Angewandte Chemie International Edition*, **48**(3), 528 (2009).
20. J. Newman and W. Tiedemann, *J. Electrochem. Soc.*, **140**, 1961 (1993).
21. J. Liu, M. Kunz, K. Chen, N. Tamura, and T. J. Richardson, *J. Phys. Chem. Lett.*, **1**, 2120 (2010).
22. P. Taheri, S. Hsieh, and M. Bahrami, *J. Power Sources*, **196**, 6525 (2011).
23. U. S. Kim, C. B. Shin, and C.-S. Kim, *J. Power Sources*, **180**, 909 (2008).
24. U. S. Kim, C. B. Shin, and C.-S. Kim, *J. Power Sources*, **189**, 841 (2009).
25. U. Seong Kim, J. Yi, C. B. Shin, T. Han, and S. Park, *J. Electrochem. Soc.*, **158**, A611 (2011).
26. S. Chacko and Y. M. Chung, *J. Power Sources*, **213**, 296 (2012).
27. J. Yi, U. S. Kim, C. B. Shin, T. Han, and S. Park, *J. Electrochem. Soc.*, **160**, A437 (2013).
28. R. E. Gerver and J. P. Meyers, *J. Electrochem. Soc.*, **158**, A835 (2011).
29. G.-H. Kim, K. Smith, K.-J. Lee, S. Santhanagopalan, and A. Pesaran, *J. Electrochem. Soc.*, **158**(8), A955 (2011).
30. M. Guo and R. E. White, *J. Power Sources*, **221**, 334 (2013).
31. W. Tiedemann and J. Newman, in: S. Gross (Ed.), *Battery design and optimization*, The Electrochemical Society Proceeding Series, Pennington, NJ, 1979, pp. 39.
32. H. Gu, *J. Electrochem. Soc.*, **130**, 1459 (1983).
33. K. H. Kwon, C. B. Shin, T. H. Kang, and C.-S. Kim, *J. Power Sources*, **163**, 151 (2006).
34. H. S. Carslaw and J. C. Jaeger, *Conduction of heat in solids*, 2nd Edition, Clarendon Press, Oxford, 1959.
35. M. N. Özisik, *Boundary value problems of heat conduction*, Dover Publications, New York, 1989.
36. T. N. Veziroglu and S. Chandra, *Thermal conductance of two-dimensional constrictions*, AIAA paper No. 68-761.
37. T. N. Veziroglu and M. A. Huerta, *Thermal conductance of two-dimensional eccentric constrictions*, NASA Interim Report.
38. W. B. Kouwenhoven and T. W. Sackett, *Welding Journal*, **28**, 468 (1949).
39. T. W. Sackett, *Contact resistance*, Ph.D. thesis, The John Hopkins University (1950).